ACS NANOSCIENCE Au
AN OPEN ACCESS JOURNAL OF THE AMERICAN CHEMICAL SOCIETY

pubs.acs.org/nanoau
Article

Impact of Cation Distribution on Photoluminescence of Ag−In−Se/ZnSe Core/Shell Nanocrystals

Published as part of ACS Nanoscience Au special issue"Advances in Energy Conversion and Storage at the Nanoscale".

Annina Moser, Olesya Yarema, Noemi Rusch, Nikola Đorđević, Weyde M. M. Lin, Deniz Bozyigit, Nuri Yazdani, Maksym Yarema,* Mathieu Luisier, and Vanessa Wood*

Cite This: ACS Nanosci. Au 2025, 5, 21−28
Read Online

ACCESS | Metrics & More | Article Recommendations | Supporting Information

ABSTRACT: Ag−In−Se/ZnSe core/shell nanocrystals exhibit good photoluminescence quantum yield (PLQY), yet intriguingly, the maximum PLQY is first reached after several days of storage. We hypothesize that this may be due to cationic rearrangement in the nanocrystal post-synthesis. To test this hypothesis, we computationally generated ternary Ag−In−Se and quaternary Ag−In−Zn−Se nanocrystals with varying degrees of cationic disorder, as quantified by the distribution of the metal cation valence electrons in the tetrahedra around Se anions. We then used density functional theory-parametrized tight-binding simulations to study the electronic structure and optical properties of these systems as a function of the homogeneity of the valence electron distribution in a tetrahedron. We found that homogeneous distribution of cations leads to a larger band gap and optical coupling, and that, in the presence of Ag_{In} or In_{Ag} antisite defects, the introduction of intermediate valence Zn cations decreases the variance in valence electrons and improves the optical properties. We further simulated the impact of a Zn-gradient shell and rearrangement of cations in the outer layers of the nanocrystals and find that diffusion of Zn into the nanocrystal and cationic rearrangement can explain the post-synthetic increase of PLQY. This work highlights the importance of developing syntheses for multinary nanocrystals that result not only in size and composition uniformity but also in nanocrystals with a uniform distribution of charge.

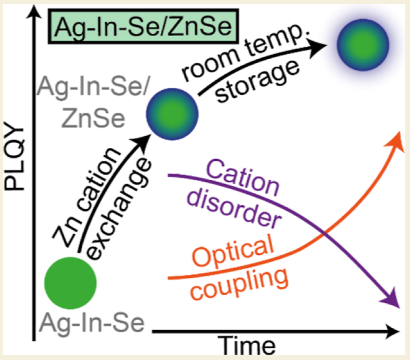

KEYWORDS: *nanocrystals, Ag−In−Se, I−III−VI, core/shell, PLQY, defect calculations, tight binding*

INTRODUCTION

Semiconductor chalcogenide nanocrystals offer a wide range of compositions with size and shape tunability,[1] tailored surfaces,[2] and the ability to form heterostructures such as core/shell nanocrystals,[3] spanning a vast library of functional materials. Historically, the first and the most studied binary chalcogenide nanocrystals contain toxic elements, such as Cd, Hg, or Pb, motivating the development of less toxic nanocrystals with more complex ternary and quaternary compositions.[4] We have previously proposed a synthesis of I−III−VI nanocrystals, utilizing amide-promotion of the nucleation stage and thus enabling a composition control of cationic ratios independently of nanocrystal size.[5−7] The additional complexity in the synthesis of I−III−VI nanocrystals due to a higher number of elements is overcompensated by an increased tunability of nanocrystal properties, where both the size and cationic ratio can be tuned.[8] In this paper, we focus on $Ag_3In_5Se_9$ nanocrystals,[9] which have a tunable photoluminescence (PL) emission spectrum between 800 and 1100 nm,[6] and are suitable for several applications including water splitting[10] and biomedical imaging.[11]

As with many nanocrystals, the growth of an inorganic shell enhances photoluminescence quantum yield (PLQY).[12] In the case of ternary $Ag_3In_5Se_9$ nanocrystals, the relatively low PLQY of approximately 20% can be significantly improved up to >70% by growing a ZnSe shell.[6] Figure 1a illustrates the core/shell synthesis via a cation exchange reaction, during which Zn ions enter into the $Ag_3In_5Se_9$ nanocrystal without a significant change of nanocrystal diameter. Consequently, the $Ag_3In_5Se_9$ core shrinks, resulting in a blue shift of the absorption with increasing shell thickness (Table S1 and Figure S1).[13] This has been confirmed by the anomalous small-angle X-ray scattering (SAXS) measurements, revealing a temperature-dependent radial Zn gradient, namely, a deeper penetration of Zn ions into the nanocrystal at higher synthesis temperatures.[14]

Received: July 28, 2024
Revised: October 22, 2024
Accepted: October 23, 2024
Published: November 4, 2024

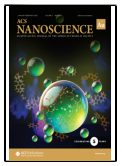

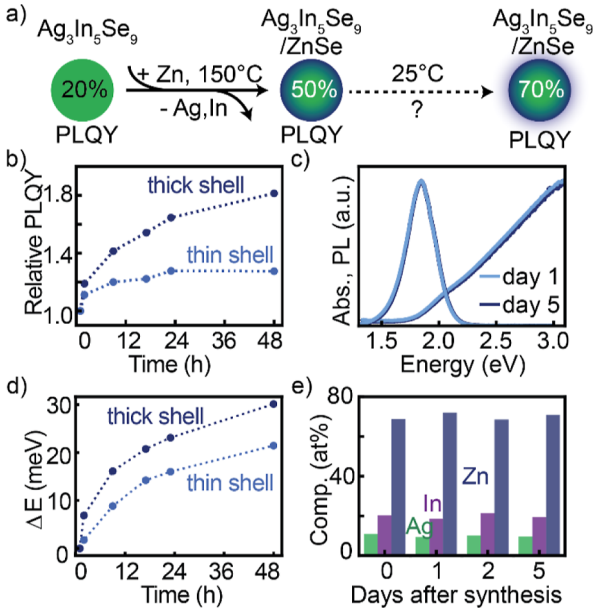

Figure 1. (a) Scheme showing PLQY evolution of $Ag_3In_5Se_9$ nanocrystals from 20% for cores to 50% immediately after growth of ZnSe shell at 150 °C and eventually to 70% following two days of storage at room temperature. (b) Evolution of the PLQY following thin and thick ZnSe shell growth at 70 and 150 °C, respectively. (c) Absorption and PL emission spectra of the $Ag_3In_5Se_9$/ZnSe (thick shell) nanocrystals after one and five days past the shell synthesis. (d) Evolution of PL energy shift following thin and thick ZnSe shell growth. (e) Elemental composition of $Ag_3In_5Se_9$/ZnSe (thick shell) nanocrystals measured each day after the shell synthesis.

However, the record PLQY values are not reached immediately after the shell growth but rather after a couple of days of storage at room temperature (Figures 1b and S2). Once reached, however, the $Ag_3In_5Se_9$/ZnSe core/shell nanocrystals maintain this high PLQY.[6]

In contrast to significant change in PLQY, we observe minor or no change of the other properties of the $Ag_3In_5Se_9$/ZnSe core/shell nanocrystals. Both absorption and PL spectra (Figure 1c) exhibit only a small blue shift during the 5 days of storage (for example, the peak PL shifts by 20−30 meV, Figures 1d and S3). Furthermore, the increase of PLQY cannot be attributed to structural changes either. For example, daily EDX measurements on fresh $Ag_3In_5Se_9$/ZnSe core/shell nanocrystals show the same composition ratios, thus excluding the post-synthetic leaching processes (Figure 1e). We therefore hypothesize that the increase in PLQY in the days following the ZnSe shell growth stems from an atomic rearrangement within the cationic lattice in a way that is favorable for radiative recombination. The significant change in PLQY can stem from multiple processes linked to radiative and nonradiative recombination, such as defect trapping or changes in vibrational coupling, which are linked to the atomic structure in the nanocrystal and thus can be best studied through theory calculations.

In this paper, we use density functional theory (DFT)-parametrized tight-binding simulations to investigate whether the observed increase in PLQY can be explained by post-synthetic cationic ordering. Previously, the PLQY of I−III−VI materials has been linked to the ordering of cations and cationic vacancies. In bulk Cu−In−Se, ordered vacancies can occur for stoichiometries described by $Cu_{n-3}In_{n+1}Se_{2n}$ with n between 4 and 9.[15] For sub-10 nm nanocrystals, these indium-rich I−III−VI compositions stand out within the broad solid solution as having particularly high PLQY.[16] Similarly, peak PLQY values manifest in indium-rich $Ag_{n-3}In_{n+1}Se_{2n}$ nanocrystals for n = 5 and 9.[6] At the same time, aliovalent chalcogenides are prone to cation disorder, which limits their optical performance.[9]

In our previous study for Cu−Zn−In−Se nanocrystals,[17] we use tight binding[18] in order to rapidly assess the effects of long-range atomic order. Here, we use a statistical approach to generate nanocrystals spanning the entire range of possible atomic arrangements to investigate the potential impact of cationic ordering on the optical properties of Ag−In−Se and Ag−Zn−In−Se nanocrystals and to simulate the effect on the optical properties for Zn diffusing within the $Ag_3In_5Se_9$/ZnSe core/shell nanocrystal. Finally, we demonstrate experimental validation of our simulations via time-dependent transient PL measurements for $Ag_3In_5Se_9$/ZnSe core/shell nanocrystals.

RESULTS

Computer-Generated Ag−In−Se Nanocrystals

In accordance with our previous work,[17] we create an expanded hexagonal unit cell containing 18 Se atoms, 2 vacancies, 6 Ag cations, and 10 In atoms (Figure 2a). We assume a fixed anion lattice, so that each Se anion is

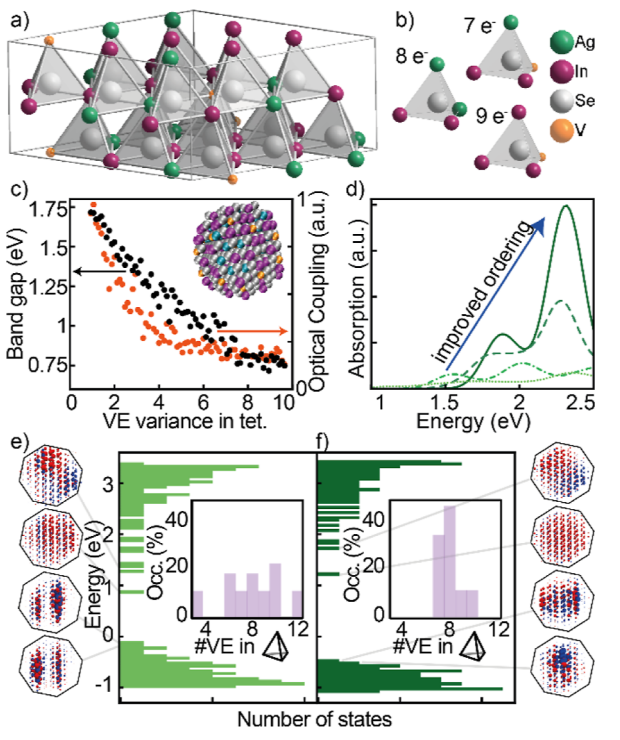

Figure 2. (a) Hexagonal unit cell of $Ag_3In_5Se_9$ ordered vacancy compound with (b) exemplary tetrahedra and corresponding number of cationic VEs. (c) Dependence of nanocrystal band gap and optical coupling strength on variance of VEs in tetrahedra. Inset: modeled $Ag_3In_5Se_9$ nanocrystal. (d) Calculated absorption spectra of nanocrystals with increasing ordering of cations (most ordered in dark green with VE variance of 0.94 and less ordered in light green with VE variances of 2.0, 3.2, and 6.7). (e) Density of states and selected wave functions (red/blue for positive/negative sign) for poorly ordered and (f) well-ordered $Ag_3In_5Se_9$ nanocrystals. Insets: distribution of VE in tetrahedra of corresponding $Ag_3In_5Se_9$ unit cells.

https://doi.org/10.1021/acsnanoscienceau.4c00045
ACS Nanosci. Au 2025, 5, 21−28

surrounded by four cations in a corner-sharing tetrahedral arrangement. Randomly assigning Ag, In, and vacancies to the 18 cationic positions in such a cell, more than one million different configurations are possible, of which we eventually eliminate duplicates due to unit cell symmetry.

The Se anion has an oxidation state of −2, which is compensated by its surrounding cations. For Ag(I), Zn(II), and In(III) metal cations, the oxidation state is equal to the number of valence electrons (VEs) of the respective elements. Since tetrahedra are corner-sharing, the ideal sum of metal VEs per tetrahedron is 8. While this is given as an average value in $Ag_3In_5Se_9$, it is not possible to satisfy this condition for each tetrahedron (Figure 2b). The number of VEs in individual tetrahedra can vary significantly. For example, the tetrahedron with two vacancies and two Ag(I) possesses 2 valent electrons, while the tetrahedron with four In(III) has 12 valent electrons. To classify the randomly generated unit cells, we extracted the number of metal VEs for the 18 tetrahedra of each unit cell and computed the statistical variance from the mean value of 8. A low variance indicates that the VE numbers in tetrahedra do not vary widely from the mean value. The smallest variance for $Ag_3Se_5In_9$ unit cells is 0.94 (Figure 2a) and may reach values up to 9.6 for most inhomogeneous distributions. A histogram of the variances for each unit cell is shown in Figure S4.

From the above computed configurations, we select one unit cell for a given value of variance, resulting in 75 distinct unit cells. We formed nanocrystals (approximately 3 nm in diameter) by expanding each of these 75 unit cells and then cutting along 100 and 110 crystal lattice planes such that each nanocrystal contains 512 atoms (Figure 2c).

Optical Properties of Ag−In−Se Nanocrystals

For each of the 75 nanocrystals, we compute the energy of electronic states and their wave functions using the OMEN package (Figure S5).[19] We also calculate the optical coupling strength between valence and conduction states and simulate the absorption spectrum by applying a Gaussian broadening of 50 meV on each transition accounting for experimentally broadened PL peaks from finite size distributions and variations in configuration.[17] We find that for all nanocrystals, the optical coupling of the valence band maximum (VBM) and conduction band minimum (CBM) is weak compared to that from valence band (VB) states to a set of triplet states slightly above the CBM, analogous to previous findings.[9] In the text below, the band gap energy refers to the electronic band gap (i.e., the energy difference between the VBM and CBM) and the optical coupling describes the sum of couplings from transitions between the highest five VB states and lowest five conduction band (CB) states (details of DFT parametrization and tight-binding parameter fitting are given in the Experimental Section and in the Supporting Information).

Band gap energies and optical couplings calculated for the nanocrystals with 75 different configurations are plotted in Figure 2c as a function of the variance in the number of VEs in tetrahedra for the respective unit cell. The optical coupling is proportional to the summed-up overlap of simulated valence and conduction band wave functions. As the average deviation from 8 VEs per tetrahedron increases, the band gap and optical coupling strength decrease. To estimate the impact of this trend and explain it, we show the simulated absorption (Figure 2d), the electronic structure, and wave functions of two nanocrystals with different distributions of VEs in tetrahedrons (Figure 2e,f). The absorption is derived from the wave function overlap and the transition energy of simulated valence and conduction band states, broadened with a Gaussian curve, and summed up over all transitions within the considered energy range. For the nanocrystal with better order, a narrower distribution of tetrahedra and more tetrahedra containing 8 VEs are characteristic (Figure 2f), and the wave functions are more symmetric and evenly distributed across the nanocrystal, leading to improved optical coupling and increased absorption. We note that the calculated band gap varies over a range of 1 eV, which is significantly larger than the experimentally observed PL peak energy shifts of 20−30 meV as an average of multiple nanocrystals. This suggests that small structural changes are already sufficient to enhance the PLQY of nanocrystals.

To understand this discrepancy, we look at the inhomogeneity in cation distribution as spatial distribution of antisite cationic defects, which are known to occur.[17] If we randomly exchange 5% of Ag with In cations in the configuration with minimal tetrahedron distribution, we find an increase in tetrahedron deviation (from 0.94 to >1.5) as well as a decrease of band gap (green data points in Figure 3a) and optical

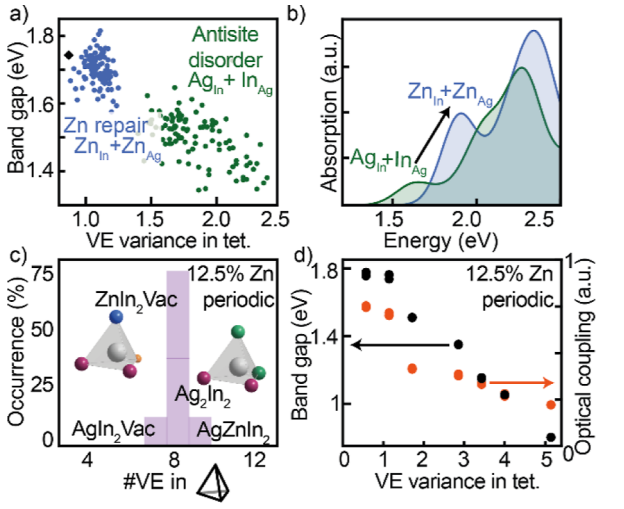

Figure 3. (a) Band gap versus variance of VE in cationic tetrahedra upon the introduction of 5% random cationic antisite defects (green) and their replacement with Zn cations (blue). The black diamond indicates the simulated nanocrystal with the optimal unit cell. (b) Calculated absorption of $Ag_3In_5Se_9$ with antisite disorder and Zn repair. (c) Tetrahedron types in $(Ag_2In_4Se_7)(ZnSe)$ with optimal VE variance in tetrahedra. (d) Dependence of band gap and optical coupling strength on VE variance in tetrahedra of $(Ag_2In_4Se_7)(ZnSe)$ nanocrystals generated from periodic unit cells.

coupling (Figure S6). We conclude that the uniformity in cationic distribution at the level of individual tetrahedra in $Ag_3In_5Se_9$ is key to the optical properties of the nanocrystal.[9] The broad PL and absorption spectra measured for these materials,[16] which cannot be fully explained by size or composition variation in the nanocrystals in the ensemble, are therefore indicative of different extents of variance in the nanocrystal assembly. We note that the impact of antisite disorder in the surface layer on the band gap and optical coupling is significantly lower than that of deeper lying layers (Figure S7). This implies that wave functions are mostly influenced by the arrangement of core atoms and may correspond to a lower wave function density in the surface layer for wave functions around the band gap.

https://doi.org/10.1021/acsnanoscienceau.4c00045
ACS Nanosci. Au 2025, 5, 21−28

Quaternary Ag−Zn−In−Se Nanocrystals

We now replace the introduced 5% antisite defects from the example above with Zn cations (i.e., Zn in In_{Ag} = Zn_{Ag} and Zn in Ag_{In} = Zn_{In}), resulting in randomly distributed Zn inside the nanocrystal (Figure 3a). This significantly reduces the variance in the distribution of VEs in tetrahedra from a mean value of 1.8 to 1.1, since adding Zn(II) in place of exchanged Ag(I) and In(III) means that the average number of VEs in tetrahedra becomes closer to 8. For example, the value of a single tetrahedron may be reduced from 10 (i.e., Se surrounded by In, In, In_{Ag}, and Ag) to 9 (In, In, Zn_{Ag}, and Ag). The electronic density across the nanocrystals also becomes more uniform with Zn replacement (Figure S8), which is reflected in an improvement of optical coupling strength and enhancement of the absorption (Figure 3b). This is consistent with experimental measurements, showing higher PLQY for quaternary Ag−In−Zn−S nanocrystals.[20]

To systematically study the behavior of quaternary Ag−In−Zn−Se, we assume a solid solution of $Ag_2In_4Se_7$ and ZnSe, such that each unit cell contains 8 Se atoms, 1 vacancy, 1 Zn atom, 2 Ag, and 4 In atoms. In this unit cell, the variance reaches numbers between 0.57 and 5.1. Interestingly, the minimal variance value of 0.57 is smaller than that achievable in ternary $Ag_3In_5Se_9$ (Figures 3c and S4b). As for the case of ternary unit cells, we compile all 840 possible configurations and model three nanocrystals of selected unit cells per given value of variance (Figure 3d). The same trend as for ternary compositions applies, revealing the largest band gaps and strongest coupling for minimal tetrahedron deviation. In the literature, we find that quaternary Ag−In−Zn−S nanocrystals have a larger band gap than Ag−In−S,[20] which is in agreement with our calculations. Furthermore, DFT calculations of Ag−In−Zn−S thin films show an increase in CB edge energy and total band gap with increasing Zn content band structures calculated, again consistent with our tight-binding simulations (Figure S9).[21]

Defect Repair in Ag−In−Se/ZnSe Core/Shell Nanocrystals

We create a gradient Ag−In−Se/ZnSe nanocrystal containing a surface layer (outer shell) with a thickness of half of a unit cell as well as an inner shell with a thickness of one unit cell. The total nanocrystal size is equal to the sizes of the simulated ternary and quaternary nanocrystals. We use an optimal arrangement of cations in the core (variance of the VE distribution equal to 0.94). For the inner shell, we employ the same unit cell and replace one Ag and one In with two Zn (11% Zn), and for the outer shell, we replace two Ag and two In with four Zn (24% Zn) by minimizing the variance in the respective modified unit cells (Figure S10 and Table S2).

To simulate nonuniform Zn distribution, in a first step, we exchange Zn cations in the shells with neighboring cations, excluding Zn diffusion into the nanocrystal core (Figure 4a). We executed and tracked 90 exchanges, leading to an antisite concentration of 42% in the layers containing Zn. This increases the variance from 1.2 to 2.1 (Figure 4b). We reverse this exchange to model a stepwise antisite defect repair by exchanging three antisite cations per time step until the original structure is restored. As the variance reduces, the band gap as well as the optical coupling and absorption increases (Figures 4c and S11).

The distribution of wave functions within the nanocrystal depends on the potential landscape of the heterostructure and affects the optical properties. To study the wave function

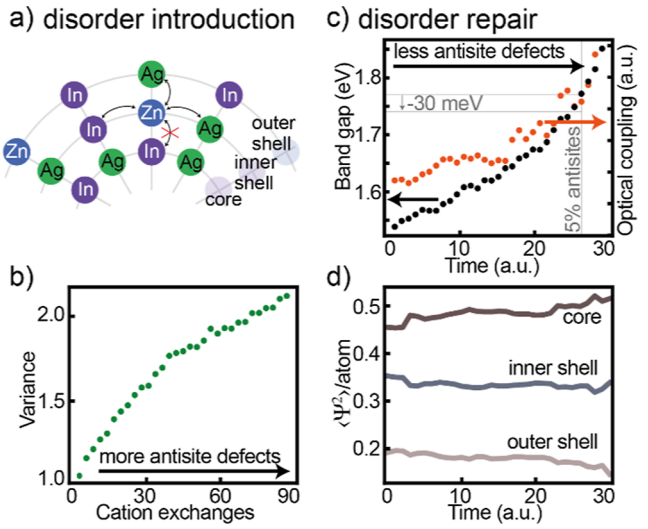

Figure 4. (a) Schematic of disorder introduction by exchange of cations in the inner and outer shells of the nanocrystal. (b) Increase in variance of VE number in tetrahedra for 90 cation exchanges. (c) Simulated recovery of band gap and optical coupling, as well as (d) increasing localization of CBM in nanocrystal core upon cationic antisite disorder repair averaged over five disordered nanocrystals. Each time step represents the exchange of three neighboring antisite cations until no antisite defects remain.

distributions in the core/shell nanocrystal, we calculate the partial wave function densities in each of three nanocrystal layers (Figure S12). The values are normalized by the number of atoms present in each layer. In the arrangement with uniform Zn distribution, approximately 50% of the CBM wave function is located in the nanocrystal core, while approximately 80% of triplet states are in the core and inner shell. Approx. 50% of VB states are localized in the inner shell of the nanocrystal (Figure S13a and Table S3).

As for homogeneous ternary and quaternary nanocrystals, disorder leads to less symmetric wave functions (Figure S13b). In particular, disorder affects the CBM wave function density distribution across the nanocrystal with more wave function density at the nanocrystal surface. Improving the valence distribution leads to a depletion of the electronic density in the outer shell and an increase of the wave function density in the nanocrystal core (Figure 4d). Similarly, we find a depletion of wave function densities of CB triplet and VB states in the outer shell (Figure S14).

DISCUSSION

Our computational findings on the impact of cationic ordering support the initial hypothesis that the origins of the PLQY increase come from Zn rearranging within the cationic sublattice of the nanocrystal (Figure 1a), resulting in a more homogeneous distribution of VEs. First, our computations predict that the cation rearrangement results in an increased band gap by 300 meV (Figure 4). Experimentally, we observe blue shifts of 30 meV for the thicker shell grown at higher temperature (150 °C) and a 20 meV shift for the thin shell grown at lower temperature (70 °C; Figure 1). This indicates that the extent of cationic rearrangement is significantly lower than simulated. In Figure 4c, we mark the configuration at which 5% of the antisite defects remain. A band gap change of 30 meV corresponds to merely one time step equivalent with three antisite defect repair steps, which in turn matches the

https://doi.org/10.1021/acsnanoscienceau.4c00045
ACS Nanosci. Au 2025, 5, 21−28

small change in absorption. While cation diffusion is relatively slow at room temperature,[22] already small changes in the crystal lattice cause significant changes of optical properties. According to previous anomalous SAXS measurements,[14] Zn is mostly present at the nanocrystal surface for low-temperature shell synthesis and diffuses deeper into the nanocrystal core during synthesis of a shell at high temperature. We also know that cation rearrangement in deeper nanocrystal layers is slower than at the surface due to a higher activation energy for diffusion.[22] According to simulations on ternary nanocrystals (Figure S7), rearrangement of cations in the nanocrystal core has a higher impact on optical properties than diffusion in the outmost layer. Taken together, this explains why the measured changes in PL and PLQY in the thick shell nanocrystal are more extensive than those in the thin shell nanocrystals (Figure 1).

Time-dependent optical spectroscopy further elucidates the post-synthetic changes. Analysis of transient PL measurements of Ag−In−Se/ZnSe core/shell nanocrystals shows two distinct recombination paths (Figures S15a and S16a).[6] The fast (approximately 10 ns) yet relatively minor contribution to luminescence is likely due to recombination between states with particularly strong optical coupling. The slower (approximately 100 ns) and dominant recombination path occurs between the valence and conduction band edges (Figure S16a).[23,24] Once excited, the hole self-traps via phonons to a lower energy state which, analogously to Cu−Zn−In−Se nanocrystals, we associate with localized VB states due to the presence of Ag and vacancies in the same tetrahedron.[17] These radiative recombination paths compete with phonon-mediated nonradiative recombination. Due to broad PL emissions, the two radiative recombination paths cannot be filtered to measure separately.

We conduct time-dependent transient PL measurements starting 1h after the end of synthesis and evaluate the collected spectra with the machine-learning LumiML algorithm to ensure nonbiased data fitting (Figures S15b,c).[25] In short, the algorithm fits the spectra to a discrete basis without a prior assumption of recombination mechanisms. The relative decay contributions remain mostly unchanged such that the PL decay may be approximated with just the slow recombination path throughout storage time. No change of recombination rate is detected (Figure S16b,c), indicating that the mechanism does not change but only the relative efficiency of the self-trapping and recombination process over other nonradiative processes. This matches previous findings that the recombination rate is dominated by nonradiative processes, which are composition-independent.[17] An increase in cationic homogeneity in nanocrystals leads to an increase in optical coupling and thus better overlap between conduction and VB states. Indeed, a comparison of recombination rates reveals a pronounced increase in the radiative recombination compared to a weaker decrease in the nonradiative recombination for both samples (Figure S17).

Furthermore, we expect a higher radiative rate of self-trapped holes in the absence of disorder analogous to calculations for Cu−Zn−In−Se nanocrystals.[17] At the same time, localizing the CBM away from the nanocrystal surface reduces the influence of potential surface defects on exciton recombination, thus favoring the dominant recombination path between the CBM and a localized state over nonradiative recombination and reducing nonradiative rate. This enables the self-trapping of more holes, resulting in an ultimate increase in radiative recombination.

In general, our findings highlight the strong effects of even small composition inhomogeneity in multinary nanocrystals, which may negatively or positively impact the optical properties. Examples of self-healing are known in nanocrystals,[26−28] and the small crystallite domains in nanocrystals promote the spontaneous return to the energetically more favorable structure with homogeneous cation distribution, which may be accelerated with a tailored annealing step.[26] In the case of the small $Ag_3In_5Se_9$/ZnSe core/shell nanocrystals studied here, we show that introduction of a cation of intermediate valence at elevated temperatures leads to a finite antisite defect concentration. Sufficiently long storage at room temperature thereby allows cation diffusion for improved PLQY.

CONCLUSIONS

DFT-parametrized tight-binding modeling of chalcogenide nanocrystals provides valuable insight into the impact of the cationic distribution and of adding a shell. In particular, we demonstrate a systematic approach to understand the optical properties of nanocrystals by looking at the statistical distribution of charge around each anion, as quantified here by the variance of the VE distribution. We note that this perspective on charge distribution is equivalent to the valence-octet or Grimm−Sommerfeld rule, which has been successfully applied to model related ternary[29,30] and quaternary[31] chalcogenide materials with aliovalent cations.

Moving forward, our findings point toward the potential to develop synthetic approaches to control cationic distributions in the nanocrystals and thereby achieve superior optical properties. On one hand, this work shows that careful selection of time and temperature promotes atomic diffusion toward a homogeneous distribution of constituent elements. Additionally, by performing studies to gain detailed understanding of reaction mechanisms and kinetics which indicate how cations enter the nanocrystal,[32] it may be possible to obtain insights into how to control cation homogeneity through the choice of precursors, concentrations, and reaction parameters.

EXPERIMENTAL METHODS

Materials and General Remarks

Silver(I) iodide (anhydrous, 99.999%) and indium(III) iodide (anhydrous, 99.999%) are purchased from Alfa-Aesar; selenium (99.99%) and tri-*n*-octylphosphine (TOP, 97%) are purchased from Strem; diethylzinc (1 M in hexane), oleic acid (techn. 90%), toluene (99.7%), ethanol (99.9%), and methanol (99.9%) are purchased from Sigma-Aldrich; lithium bis(trimethylsilyl)amide ($LiN(SiMe_3)_2$, 95%) and oleylamine (80−90%) are purchased from Acros. $LiN(SiMe_3)_2$ is recrystallized from a hexane solution at −20 °C. Oleylamine and oleic acid are purified from water residues by heating to 100 °C under vacuum for at least 1 h and then transferred into the glovebox. All other chemicals are used as received. Stock solutions of silver(I) iodide (0.25 M), indium(III) iodide, and Se (1 M), as well as $LiN(SiMe_3)_2$ (approximately 1.6 M) are prepared. Injection mixtures and stock solutions are prepared in a N_2-filled glovebox. All syntheses are carried out in an air-free environment using the standard Schlenk line technique.

Synthesis of Nanocrystals

The synthesis and purification of ternary Ag−In−Se as well as the growth of ZnSe shell via a cation exchange are described in detail in previous publications.[5,6] The temperature of the thin ZnSe shell

https://doi.org/10.1021/acsnanoscienceau.4c00045
ACS Nanosci. Au 2025, 5, 21−28

growth synthesis is kept at 70 °C, while 150 °C is used for the thick ZnSe shell.

Basic Characterization

TEM images are acquired on a Hitachi HT7700 and on a JEOL JEM-1400 Plus, both operating at 100 keV. Size distributions are evaluated by measuring >100 particles per sample with ImageJ software. Energy-dispersive X-ray spectroscopy (EDX) data are measured with FEI Quanta 200 FEG SEM microscopes, operating at 30 keV. Absorption spectra are obtained with an Agilent Cary 5000 UV−vis−NIR spectrophotometer by measuring diluted nanocrystals in tetrachloroethylene. For PL and PLQY, diluted nanocrystals are illuminated with blue lasers (405 nm, World star, 10 mW; 450 nm, Thorlabs, 5 mW), and the signal is recorded with an Ocean Optics QE65000 spectrometer. PLQY of core/shell nanocrystals is measured repeatedly for two days starting 1 h after synthesis completion. Quantum yield values are computed according to the published protocol[33] using rhodamine B in ethanol as a reference solution.[34]

Transient Photoluminescence and LumiML

Core/shell nanocrystals dissolved in toluene are placed in a 1 mm thick quartz cuvette and illuminated for 20 s with a picosecond pulsed laser (405 nm, Hamamatsu C10196) over 44 h with 40 min intervals, starting 1 h after synthesis completion. The transient photoluminescence signal is collected with an avalanche photodetector (Excelitas Technologies, SPCM-AQRH-TR). Significant signal decay is noticed after 20 h, and measurements beyond this time are discarded.

Transient photoluminescence spectra are analyzed with LumiML, a python-based machine-learning software.[25] The same starting parameter set is used for all measurements of one sample. A histogram basis over a decay frequency range between 0.002 ns^{-1} and 0.49 nm^{-1} with logarithmic spacing (total of 17 frequency points) is used with an ω of 3π and five cross validation steps per measurement.

Band Structures of $AgInSe_2$, $ZnInSe_2$, and Vacancy Compound

DFT + GGA calculations are performed with the Vienna ab initio simulation package[35−38] using HSE06 hybrid functionals to accurately reproduce the band gap.[39] Tetragonal chalcopyrite unit cells of $AgInSe_2$, $ZnInSe_2$, and $CuIn_2Se_4$ are fully relaxed (ionically relaxed for $CuIn_2Se_4$ containing one vacancy), and electronic and ionic potentials are optimized for a grid of 8 × 8 × 8 *k*-points (4 × 4 × 4 *k*-points for $CuIn_2Se_4$) with Perdew−Burke−Ernzerhof functional. Spin polarization is not considered. The cutoff energy for the plane wave basis set is set to 350 eV (500 eV for $CuIn_2Se_4$). The break condition is set to 10^{-6} for the self-consistent iterative calculation and 10^{-5} for the conjugate-gradient algorithm of ionic relaxation. $AgInSe_2$ has calculated lattice parameters a of 6.149 Å, η of 1.9284, u of 0.258852, and a band gap of 1.24 eV, matching previous studies.[40]

Tight-Binding Parametrization

For tight binding, only localized orthogonal wave functions and nearest neighbor interactions are considered. Cu, Ag, Zn, and vacancies are modeled with a sp^3d^5 atomic orbital configuration, while In and Se are represented with sp^3. Least squares fittings are applied to the DFT band structures. In−Se bonds are computed globally to ensure consistency. The parameters (Table S4) are added to OMEN for nanocrystal calculations. Since $ZnInSe_2$ is an artificial composition, Zn may be introduced as a dopant with concentrations up to 25% of cations.

Nanocrystals are created by first expanding the relaxed unit cell to a bulk structure and then carving out a crystal with well-defined cutting planes along (100) and (110). Tight-binding simulations are performed with the OMEN tools[19] using 100 eV dsp^3 hybridization for dangling bonds.[41]

The outputs include the top VB and bottom CB as well as the corresponding wave functions and the CB−VB optical coupling matrix. The optical coupling figure of merit is defined to be the total coupling strength of the first five valence and conduction band states. The output of the OMEN is evaluated with Mathematica and MATLAB software.

ASSOCIATED CONTENT

Supporting Information

The Supporting Information is available free of charge at https://pubs.acs.org/doi/10.1021/acsnanoscienceau.4c00045.

Experimental data for nanocrystals, PL quantum yield and steady-state PL as a function of storage time, computational results for nanocrystals, density of states, optical coupling, variance of valent electrons in tetrahedra, wave functions, calculated absorption spectra, transient PL data with machine-learning fits, and tight-binding parameters (PDF)

AUTHOR INFORMATION

Corresponding Authors

Maksym Yarema − *Institute for Electronics, Department of Information Technology and Electrical Engineering, ETH Zurich, Zurich CH-8092, Switzerland;* orcid.org/0000-0002-2006-2466; Email: yaremam@ethz.ch

Vanessa Wood − *Institute for Electronics, Department of Information Technology and Electrical Engineering, ETH Zurich, Zurich CH-8092, Switzerland;* orcid.org/0000-0001-6435-0227; Email: vwood@ethz.ch

Authors

Annina Moser − *Institute for Electronics, Department of Information Technology and Electrical Engineering, ETH Zurich, Zurich CH-8092, Switzerland*

Olesya Yarema − *Institute for Electronics, Department of Information Technology and Electrical Engineering, ETH Zurich, Zurich CH-8092, Switzerland;* orcid.org/0000-0002-1653-1338

Noemi Rusch − *Institute for Electronics, Department of Information Technology and Electrical Engineering, ETH Zurich, Zurich CH-8092, Switzerland*

Nikola Đorđević − *Institute for Electronics, Department of Information Technology and Electrical Engineering, ETH Zurich, Zurich CH-8092, Switzerland*

Weyde M. M. Lin − *Institute for Electronics, Department of Information Technology and Electrical Engineering, ETH Zurich, Zurich CH-8092, Switzerland*

Deniz Bozyigit − *Institute for Electronics, Department of Information Technology and Electrical Engineering, ETH Zurich, Zurich CH-8092, Switzerland*

Nuri Yazdani − *Institute for Electronics, Department of Information Technology and Electrical Engineering, ETH Zurich, Zurich CH-8092, Switzerland;* orcid.org/0000-0001-6593-7601

Mathieu Luisier − *Institute for Integrated Systems, Department of Information Technology and Electrical Engineering, ETH Zurich, Zurich CH-8092, Switzerland;* orcid.org/0000-0002-2212-7972

Complete contact information is available at: https://pubs.acs.org/10.1021/acsnanoscienceau.4c00045

Author Contributions

The manuscript was written through the contributions of all authors. CRediT: **Annina Moser** data curation, formal analysis, investigation, methodology, visualization, writing - original

https://doi.org/10.1021/acsnanoscienceau.4c00045
ACS Nanosci. Au 2025, 5, 21−28

draft, writing - review & editing; **Olesya Yarema** data curation, formal analysis, investigation, methodology; **Noemi Rusch** data curation, formal analysis, investigation; **Nikola Đorđević** data curation, formal analysis, investigation; **Weyde M. M. Lin** data curation, formal analysis, investigation; **Deniz Bozyigit** data curation, formal analysis, investigation; **Nuri Yazdani** formal analysis, investigation, methodology, validation; **Maksym Yarema** conceptualization, funding acquisition, investigation, methodology, supervision, validation, writing - original draft, writing - review & editing; **Mathieu Luisier** conceptualization, methodology, supervision, validation, writing - original draft, writing - review & editing; **Vanessa Wood** conceptualization, funding acquisition, methodology, supervision, validation, writing - original draft, writing - review & editing.

Funding

V.W. acknowledges funding from the Swiss National Science Foundation (SNSF grant no. 175889), M.Y. acknowledges funding from the European Research Council (ERC) under the European Union's Horizon 2020 research and innovation program (grant agreement no. 852751).

Notes

The authors declare no competing financial interest.

■ ACKNOWLEDGMENTS

In memory of N.R., who successfully performed her Bachelor's thesis investigating cationic order and who passed away well before her time in Spring 2022. The authors thank Alexandra Turrini and Petr Khomyakov for DFT and tight-binding parameter calculations and Mario Mücklich for technical lab assistance. TEM, STEM, and EDX measurements were performed at the Scientific Center for Optical and Electron Microscopy (ScopeM) of the Swiss Federal Institute of Technology, Zurich. Analysis of transient photoluminescence with LumiML software was performed on the EULER (Erweiterbarer, Umweltfreundlicher, Leistungsfähiger ETH-Rechner) multicore cluster.

■ REFERENCES

(1) Burda, C.; Chen, X.; Narayanan, R.; El-Sayed, M. A. Chemistry and Properties of Nanocrystals of Different Shapes. *Chem. Rev.* **2005**, *105*, 1025−1102.
(2) Heuer-Jungemann, A.; Feliu, N.; Bakaimi, I.; Hamaly, M.; Alkilany, A.; Chakraborty, I.; Masood, A.; Casula, M. F.; Kostopoulou, A.; Oh, E.; Susumu, K.; Stewart, M. H.; Medintz, I. L.; Stratakis, E.; Parak, W. J.; Kanaras, A. G. The Role of Ligands in the Chemical Synthesis and Applications of Inorganic Nanoparticles. *Chem. Rev.* **2019**, *119*, 4819−4880.
(3) Ghosh Chaudhuri, R.; Paria, S. Core/Shell Nanoparticles: Classes, Properties, Synthesis Mechanisms, Characterization, and Applications. *Chem. Rev.* **2012**, *112*, 2373−2433.
(4) Reiss, P.; Carrière, M.; Lincheneau, C.; Vaure, L.; Tamang, S. Synthesis of Semiconductor Nanocrystals, Focusing on Nontoxic and Earth-Abundant Materials. *Chem. Rev.* **2016**, *116*, 10731−10819.
(5) Yarema, O.; Bozyigit, D.; Rousseau, I.; Nowack, L.; Yarema, M.; Heiss, W.; Wood, V. Highly Luminescent, Size- and Shape-Tunable Copper Indium Selenide Based Colloidal Nanocrystals. *Chem. Mater.* **2013**, *25*, 3753−3757.
(6) Yarema, O.; Yarema, M.; Bozyigit, D.; Lin, W. M. M.; Wood, V. Independent Composition and Size Control for Highly Luminescent Indium-Rich Silver Indium Selenide Nanocrystals. *ACS Nano* **2015**, *9*, 11134−11142.
(7) Yarema, O.; Yarema, M.; Lin, W. M. M.; Wood, V. Cu−In−Te and Ag−In−Te Colloidal Nanocrystals with Tunable Composition and Size. *Chem. Commun.* **2016**, *52*, 10878−10881.
(8) Heo, J.; Dumett Torres, D.; Jain, P. K. Unconventional Long-Range Cation Ordering in Copper Selenide Nanocrystals. *Chem. Mater.* **2019**, *31*, 68−72.
(9) Zacharia, A.; Papagiorgis, P.; Yarema, O.; Moser, A.; Othonos, A.; Luisier, M.; Wood, V.; Yarema, M.; Itskos, G. Optical Transitions in Silver Indium Selenide Nanocrystals: Implications for Light-Emitting and Light-Imaging Applications. *ACS Appl. Nano Mater.* **2021**, *4*, 11239−11248.
(10) Ganguly, P.; R, S. K.; Muscetta, M.; Padmanabhan, N. T.; Clarizia, L.; Akande, A.; Hinder, S.; Mathew, S.; John, H.; Breen, A.; Pillai, S. C. New Insights into the Efficient Charge Transfer of Ternary Chalcogenides Composites of TiO_2. *Appl. Catal. B Environ.* **2021**, *282*, 119612.
(11) Che, D.; Zhu, X.; Wang, H.; Duan, Y.; Zhang, Q.; Li, Y. Aqueous Synthesis of High Bright and Tunable Near-Infrared $AgInSe_2$−ZnSe Quantum Dots for Bioimaging. *J. Colloid Interface Sci.* **2016**, *463*, 1−7.
(12) Reiss, P.; Protière, M.; Li, L. Core/Shell Semiconductor Nanocrystals. *Small* **2009**, *5*, 154−168.
(13) De Trizio, L.; Manna, L. Forging Colloidal Nanostructures via Cation Exchange Reactions. *Chem. Rev.* **2016**, *116*, 10852−10887.
(14) Yarema, M.; Xing, Y.; Lechner, R. T.; Ludescher, L.; Dordevic, N.; Lin, W. M. M.; Yarema, O.; Wood, V. Mapping the Atomistic Structure of Graded Core/Shell Colloidal Nanocrystals. *Sci. Rep.* **2017**, *7*, 11718.
(15) Wasim, S. M.; Rincón, C.; Marin, G.; Delgado, J. M.; Contreras, J. Effect of Ordered Defects on the Crystal Structure of In-Rich Ternary Compounds of the Cu-In-Se System. *J. Phys. D Appl. Phys.* **2004**, *37*, 479−484.
(16) Allen, P. M.; Bawendi, M. G. Ternary I-III-VI Quantum Dots Luminescent in the Red to Near-Infrared. *J. Am. Chem. Soc.* **2008**, *130*, 9240−9241.
(17) Yarema, M.; Yazdani, N.; Yarema, O.; Đorđević, N.; Lin, W. M. M.; Bozyigit, D.; Volk, S.; Moser, A.; Turrini, A.; Khomyakov, P. A.; Nachtegaal, M.; Luisier, M.; Wood, V. Structural Ordering in Ultrasmall Multicomponent Chalcogenides: The Case of Quaternary Cu-Zn-In-Se Nanocrystals. *Adv. Mater.* **2024**, 2406351.
(18) Keuleyan, S. E.; Guyot-Sionnest, P.; Delerue, C.; Allan, G. Mercury Telluride Colloidal Quantum Dots: Electronic Structure, Size-Dependent Spectra, and Photocurrent Detection up to 12 Mm. *ACS Nano* **2014**, *8*, 8676−8682.
(19) Luisier, M.; Schenk, A.; Fichtner, W.; Klimeck, G. Atomistic Simulation of Nanowires in the $sp^3d^5s^*$ Tight-Binding Formalism: From Boundary Conditions to Strain Calculations. *Phys. Rev. B* **2006**, *74*, 205323.
(20) Song, J.; Ma, C.; Zhang, W.; Li, X.; Zhang, W.; Wu, R.; Cheng, X.; Ali, A.; Yang, M.; Zhu, L.; Xia, R.; Xu, X. Bandgap and Structure Engineering via Cation Exchange: From Binary Ag_2S to Ternary $AgInS_2$, Quaternary AgZnInS Alloy and AgZnInS/ZnS Core/Shell Fluorescent Nanocrystals for Bioimaging. *ACS Appl. Mater. Interfaces* **2016**, *8*, 24826−24836.
(21) Kim, E. M.; Ruankham, P.; Lee, J. H.; Hachiya, K.; Sagawa, T. Ag-In-Zn-S Quantum Dots for Hybrid Organic-Inorganic Solar Cells. *Jpn. J. Appl. Phys.* **2016**, *55*, 02BF06.
(22) Moser, A.; Yarema, M.; Lin, W. M. M.; Yarema, O.; Yazdani, N.; Wood, V. In Situ Monitoring of Cation-Exchange Reaction Shell Growth on Nanocrystals. *J. Phys. Chem. C* **2017**, *121*, 24345−24351.
(23) Knowles, K. E.; Nelson, H. D.; Kilburn, T. B.; Gamelin, D. R. Singlet-Triplet Splittings in the Luminescent Excited States of Colloidal Cu^+:CdSe, Cu^+:InP, and $CuInS_2$ Nanocrystals: Charge-Transfer Configurations and Self-Trapped Excitons. *J. Am. Chem. Soc.* **2015**, *137*, 13138−13147.
(24) Raievska, O.; Stroyuk, O.; Dzhagan, V.; Solonenko, D.; Zahn, D. R. T. Ultra-Small Aqueous Glutathione-Capped Ag−In−Se Quantum Dots: Luminescence and Vibrational Properties. *RSC Adv.* **2020**, *10*, 42178−42193.

(25) Đorđević, N.; Beckwith, J. S.; Yarema, M.; Yarema, O.; Rosspeintner, A.; Yazdani, N.; Leuthold, J.; Vauthey, E.; Wood, V. Machine Learning for Analysis of Time-Resolved Luminescence Data. *ACS Photonics* **2018**, *5*, 4888−4895.
(26) Wang, Y.; Kavanagh, S. R.; Burgués-Ceballos, I.; Walsh, A.; Scanlon, D.; Konstantatos, G. Cation Disorder Engineering Yields $AgBiS_2$ Nanocrystals with Enhanced Optical Absorption for Efficient Ultrathin Solar Cells. *Nat. Photon.* **2022**, *16*, 235−241.
(27) Puzder, A.; Williamson, A. J.; Gygi, F.; Galli, G. Self-Healing of CdSe Nanocrystals: First-Principles Calculations. *Phys. Rev. Lett.* **2004**, *92*, 217401.
(28) Khalfin, S.; Veber, N.; Dror, S.; Shechter, R.; Shaek, S.; Levy, S.; Kauffmann, Y.; Klinger, L.; Rabkin, E.; Bekenstein, Y.; Khalfin, S.; Veber, N.; Dror, S.; Shechter, R.; Shaek, S.; Levy, S.; Kauffmann, Y.; Klinger, L.; Rabkin, E.; Bekenstein, Y. Self-Healing of Crystal Voids in Double Perovskite Nanocrystals Is Related to Surface Passivation. *Adv. Funct. Mater.* **2022**, *32*, 2110421.
(29) Miller, A.; MacKinnon, A.; Weaire, D. Beyond the Binaries-The Chalcopyrite and Related Semiconducting Compounds. *Solid State Phys. Adv. Res. Appl.* **1982**, *36*, 119−175.
(30) Shen, X.; Hernández-Pagan, E. A.; Zhou, W.; Puzyrev, Y. S.; Idrobo, J. C.; Macdonald, J. E.; Pennycook, S. J.; Pantelides, S. T. Interlaced Crystals Having a Perfect Bravais Lattice and Complex Chemical Order Revealed by Real-Space Crystallography. *Nat. Commun.* **2014**, *5*, 5431.
(31) Chen, S.; Walsh, A.; Luo, Y.; Yang, J. H.; Gong, X. G.; Wei, S. H. Wurtzite-Derived Polytypes of Kesterite and Stannite Quaternary Chalcogenide Semiconductors. *Phys. Rev. B Condens. Matter Mater. Phys.* **2010**, *82*, 195203.
(32) Moser, A.; Yarema, O.; García, G.; Luisier, M.; Longo, F.; Billeter, E.; Borgschulte, A.; Yarema, M.; Wood, V. Synthesis and Electronic Structure of Mid-IR Absorbing Cu_3SbSe_4 and Cu_xSbSe_4 Nanocrystals. *Chem. Mater.* **2023**, *35*, 6323−6331.
(33) de Mello, J. C.; Wittmann, H. F.; Friend, R. H. An Improved Experimental Determination of External Photoluminescence Quantum Efficiency. *Adv. Mater.* **1997**, *9*, 230−232.
(34) Chen, B.; Zhong, H.; Zhang, W.; Tan, Z.; Li, Y.; Yu, C.; Zhai, T.; Bando, Y.; Yang, S.; Zou, B. Highly Emissive and Color-Tunable $CuInS_2$-Based Colloidal Semiconductor Nanocrystals: Off-Stoichiometry Effects and Improved Electroluminescence Performance. *Adv. Funct. Mater.* **2012**, *22*, 2081−2088.
(35) Kresse, G.; Hafner, J. *Ab Initio* Molecular Dynamics for Liquid Metals. *Phys. Rev. B* **1993**, *47*, 558−561.
(36) Kresse, G.; Hafner, J. *Ab Initio* Molecular-Dynamics Simulation of the Liquid-Metal−Amorphous-Semiconductor Transition in Germanium. *Phys. Rev. B* **1994**, *49*, 14251−14269.
(37) Kresse, G.; Furthmüller, J. Efficient Iterative Schemes for *Ab Initio* Total-Energy Calculations Using a Plane-Wave Basis Set. *Phys. Rev. B* **1996**, *54*, 11169−11186.
(38) Kresse, G.; Furthmüller, J. Efficiency of Ab-Initio Total Energy Calculations for Metals and Semiconductors Using a Plane-Wave Basis Set. *Comput. Mater. Sci.* **1996**, *6*, 15−50.
(39) Xiao, H.; Tahir-Kheli, J.; Goddard, W. A. Accurate Band Gaps for Semiconductors from Density Functional Theory. *J. Phys. Chem. Lett.* **2011**, *2*, 212−217.
(40) Wang, L.; Ying, P.; Deng, Y.; Zhou, H.; Du, Z.; Cui, J. Site Occupations of Zn in $AgInSe_2$-Based Chalcopyrites Responsible for Modified Structures and Significantly Improved Thermoelectric Performance. *RSC Adv.* **2014**, *4*, 33897−33904.
(41) Lee, S.; Oyafuso, F.; Von Allmen, P.; Klimeck, G. Boundary Conditions for the Electronic Structure of Finite-Extent Embedded Semiconductor Nanostructures. *Phys. Rev. B* **2004**, *69*, 045316.

https://doi.org/10.1021/acsnanoscienceau.4c00045
ACS Nanosci. Au 2025, 5, 21−28